Research Article Vol. 30, No. 25 / 5 Dec 2022 / Optics Express 44640
Optics EXPRESS

Characterization of noise regimes in mid-IR free-space optical communication based on quantum cascade lasers

MARCO SEMINARA,[1,2,5] TECLA GABBRIELLI,[1,2,5] NICOLA CORRIAS,[1,2,3] SIMONE BORRI,[1,2] LUIGI CONSOLINO,[1,2] MARCO MEUCCI,[2,4] PAOLO DE NATALE,[1,2] FRANCESCO CAPPELLI,[1,2] AND JACOPO CATANI[1,2,*]

[1]*European Laboratory for Non-Linear Spectroscopy (LENS), Sesto Fiorentino (FI), Italy*
[2]*National Institute of Optics-CNR (CNR-INO), Sesto Fiorentino (FI), Italy*
[3]*QTI s.r.l., Largo E. Fermi 6, 50125 Firenze, Italy*
[4]*ARTES4.0 Competence Center on Robotics and Digital Technologies, Node of Sesto Fiorentino (FI), Italy*
[5]*These authors contributed equally to this work*
[*]*jacopo.catani@ino.cnr.it*

Abstract: The recent development of Quantum Cascade Lasers (QCLs) represents one of the biggest opportunities for the deployment of a new class of Free Space Optical (FSO) communication systems working in the mid-infrared (mid-IR) wavelength range. As compared to more common FSO systems exploiting the telecom range, the larger wavelength employed in mid-IR systems delivers exceptional benefits in case of adverse atmospheric conditions, as the reduced scattering rate strongly suppresses detrimental effects on the FSO link length given by the presence of rain, dust, fog, and haze. In this work, we use a novel FSO testbed operating at 4.7 μm, to provide a detailed experimental analysis of noise regimes that could occur in realistic FSO mid-IR systems based on QCLs. Our analysis reveals the existence of two distinct noise regions, corresponding to different realistic channel attenuation conditions, which are precisely controlled in our setup. To relate our results with real outdoor configurations, we combine experimental data with predictions of an atmospheric channel loss model, finding that error-free communication could be attained for effective distances up to 8 km in low visibility conditions of 1 km. Our analysis of noise regimes may have a key relevance for the development of novel, long-range FSO communication systems based on mid-IR QCL sources.

1. Introduction

Free-Space Optical (FSO) links represent a valuable option when the implementation of fiber links is impractical and realizing point-to-point or satellite-assisted communication infrastructures are much more efficient and convenient [1]. The technological research on Free-Space Optical Communication Systems (FSOCSs) and reinforcement of the existing infrastructures pave the way not only to the possible replacement of fiber cables in the rising 5G networks [2,3], but also to the development of new technology for the upcoming 6G era, where the implementation of a hybrid FSO/microwave platform can open new horizons for telecommunications [4,5]. Furthermore, indoor optical wireless communication can benefit from the improvement of laser-based FSO technology exploiting the advantages of a higher frequency of the carrier, a wider bandwidth, a much higher spatial directionality, unlicensed operation, high security compared to radio frequencies together with lower costs, and simpler infrastructure with respect to fiber links [6,7].

Commonly, FSOCSs have been tested and developed in the near infrared (NIR) wavelength range (0.75 μm to 3 μm), and in particular in the so-called telecom wavelength sub-range (1.55 μm) [8], on which the worldwide fiber-based communication infrastructure is currently set. The NIR

#470031 https://doi.org/10.1364/OE.470031
Journal © 2022 Received 12 Jul 2022; revised 1 Sep 2022; accepted 18 Sep 2022; published 22 Nov 2022

Optics EXPRESS

spectral region is equipped with well-established technologies on both transmitter and receiver sides (e.g., around 800 nm, with silicon detectors or high-power sources such as VCSEL). In the last decades, another spectral region has started to be attractive in terms of FSO links, the mid infrared range (mid-IR, λ>3 μm) [8], as mid-IR atmospheric transparency windows can usefully complement the NIR ones. One of the most attractive features of the mid-IR is its reduced sensitivity to particle scattering, scintillation, and background noise due to the black-body emission of the Sun (peaked at $\lambda \sim 500$ nm and well suppressed above 3 μm) [9,10]. Moreover, the high transparency windows around 4.0 μm goes along with a strongly reduced black-body emission of Earth, which is peaked at $\lambda \sim 10$ μm and is well suppressed for λ<5 μm [9]. In the mid-IR, it is also possible to achieve larger transmission efficiency than in the NIR in case of adverse weather conditions (fog, haze, clouds) [10,11], which is relevant also for satellite [12] and deep-space communications [13].

In this scenario, the advent of Quantum Cascade Lasers (QCLs) with highly-tailorable emission covering the 3 μm to 12 μm range [9,14–17], represented a technological breakthrough for extensive development of mid-IR FSOCSs. Since their invention, the attention of the communication community has been attracted by the very short lifetime (< 1 ps) of their lasing transitions, which allow both electrical and optical modulation of the emitted radiation at high frequencies (up to several GHz) [18,19]. Typically used as spectroscopy sources [20,21], mid-IR QCLs started to be tested also as transmitters in FSO communications [11,22,23]. Besides initial proof-of-concept FSOCSs embedding QCLs emitting around 4.7 μm have been reported for distances of about 2 m [24,25], recent years saw a massive development of directly-modulated QCL FSOCS working in such favorable wavelength range [26,27]. Such effort recently culminated in the capability to attain multi-Gbps bitrates with room-temperature QCLs [28], and the 10-Gbps threshold has recently been overcome by employing 9 μm QCL sources [29]. Indeed, the effective deployment of reliable mid-IR FSOCSs based on QCLs in realistic environments requires that the various noise contributions, which depend on the specific application, are analyzed and evaluated. In this sense, a theoretical model and simulations to study the transmission rate under various atmospheric conditions have been recently proposed [30], considering two different laser sources (1.55 μm and 4.0 μm) and a fixed distance of 4 km. Recently, a novel study on QCL-based FSOC has shown the BER trend as a function of the optical losses [26]. Nonetheless, a thorough experimental characterization of the impact of different noise conditions on the communication performances of a mid-IR FSO link is still lacking.

To tackle this issue, in this work we exploit a novel testbed, based on a QCL emitting at 4.72 μm to characterize, for the first time, the occurrence of two distinct noise regimes, corresponding to different, realistic conditions of channel attenuation. In particular, the experimentally analyzed noise regimes are a high attenuation noise regime (HAR), when the signal at the receiver is deeply attenuated due to, e.g., adverse weather conditions, and a low attenuation regime (LAR), that may occur in indoor wireless communication, short- and mid-range FSO links in good weather conditions. We analyze for the first time the performances of a QCL-based mid-IR FSOCS in such regimes, highlighting very different behavior for the communication quality as a function of several experimental parameters. Thanks to the tunability of the presented setup, we also explore an intermediate noise regime, observing a clear transition in the packet error rate (PER) trend as the two noise regions are spanned. By combining our findings with the predictions of an atmospheric propagation model, presented in the theoretical overview, we also estimate reliable mid-IR FSO communications for our system covering distances up to 8 km in scarce visibility conditions (1 km).

2. Setup overview

The mid-IR communication system we employ for the characterization of the noise regimes is composed of two distinct units: the transmitter unit (TX), where a digital message is encoded

Optics EXPRESS

in the light emitted by the mid-IR source through amplitude modulation (AM) via a current modulation provided by the current driver, and the receiver stage (RX), where the optical signal is detected, converted to voltage, and digitally processed for message decoding (see Fig. 1(a)).

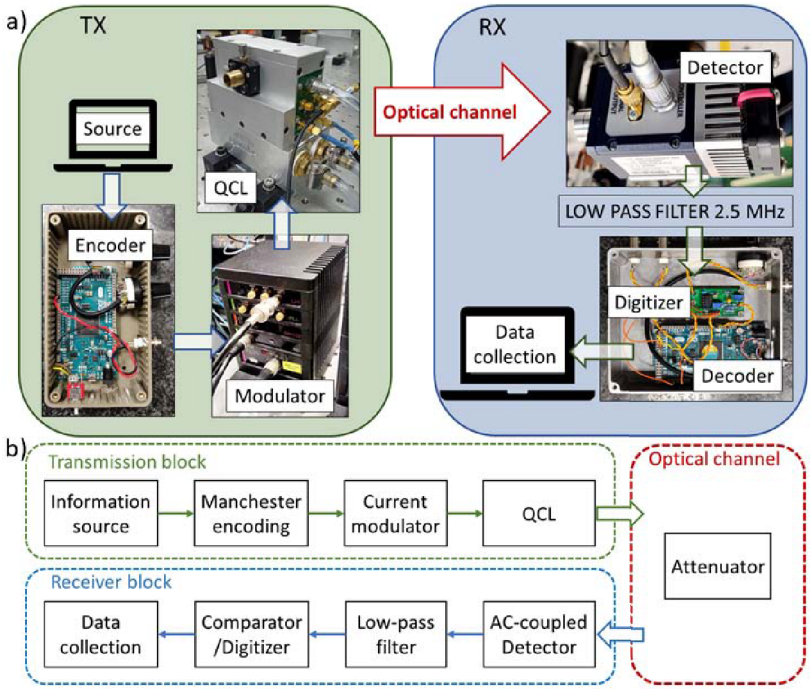

Fig. 1. Sketch (a) and block diagram (b) of the experimental setup divided into transmission block (green), optical channel (red), and receiver block (blue).

The modulated mid-IR light propagates in free space passing through a variable optical attenuation system that simulates long-distance channel losses similar to [26], reporting BER characterization for optical attenuation not exceeding 30 dB. An AC-coupled amplified detector collects the light at the receiver side. The amplified analog signal is first digitized by a variable-threshold comparator stage. Then, it is decoded and analyzed by the digital RX platform, performing a real-time comparison with a pre-stored reference message. In the following sections, details on both the TX-RX stages and the experimental setup are given.

2.1. Optical signal generation, controlled attenuation, and detection

The FSOCS source is a custom Fabry-Pérot continuous-wave QCL fabricated at ETH (Swiss Federal Institute of Technology Zurich, Switzerland), with an emitting wavelength of $\lambda = 4.72$ μm, and working at room temperature (T =18 °C). The laser works in single-mode regime from threshold current (638 mA) up to 680 mA, while for I>680 mA it operates in multi-mode regime. The maximum output optical power achievable in single-mode regime is 21 mW, with a driving current of 680 mA. The laser is powered by an ultra-low-noise current driver (QubeCL15-P from ppqSense srl), characterized by a nominal current noise density of 200 pA/$\sqrt{\text{Hz}}$. The current driver is equipped with a low-noise current modulator characterized by a maximum modulation amplitude of 5 mA and a modulation bandwidth of 0.3 MHz. The beam propagates indoor in free-space travelling an optical path length of 3 m until it reaches the RX. The beam passes through a variable optical attenuator for simulating different attenuation regimes that can occur in a long-distance outdoor FSO communication (Secs. 3 and 4). By exploiting the

Optics EXPRESS

linear polarization of the laser light, a variable attenuation is achieved via precise adjustment of a rotating polarizer plate (WP25H-Z holographic wire grid polarizer by Thorlabs). The attenuation used in the characterization covers the range from 14 dB to 52 dB (Sec. 5) [31]. After free-space propagation, the beam is focused on a two-stage transimpedance preamplified mid-IR HgCdTe photovoltaic detector (detector PVI-4TE-5-2x2, preamplifier MIP-10-250M-F-M4 both from Vigo System). The detector has a nominal bandwidth of 180 MHz and operates in the wavelength range from 2.5 µm to 5 µm. At 4.72 µm, the detector saturation occurs for an incident power of 1.2 mW and its measured quantum efficiency is 33 % [32]. The detector is used in the linear responsivity regime (for P<1.2 mW) where the output current is directly proportional to the incident flux of photons. The sensitivity limit of the detection system is given by the detector dark current.

2.2. Implementation of the digital communication signal

The used hardware is represented in Fig. 1(a) and it is composed of a TX unit (green block) and an RX unit (blue block). The digital data stream is generated by a digital open-source low-cost microcontroller board (Arduino DUE, the *Encoder* in Fig. 1(a)). Arduino DUE is a convenient open-source platform, based on a 32-bit core (ARM Cortex-M3) with 84-MHz clock, featuring remarkable processing capabilities with reduced cost and size. An on-off keying (OOK) scheme with Manchester encoding [33] is used, which guarantees a constant-average signal. The system can transmit a continuous data stream of 62500 packets with a baud rate up to 115 kbaud. Larger baud rates could easily be attained by applying a direct modulation to the QCL chip through a bias-tee. This was not feasible in the present configuration, as the QCL packaging doesn't allow for direct insertion of on-board bias-tee components. However, this is not limiting the breadth of the results on noise characterization. The packets are composed of 9 bytes, divided into 3 initial equalization bytes for signal pre-equalization, 2 synchronization bytes, and 4 data payload bytes. The digital information is encoded in the beam as intensity modulation via the current driver which adds AC modulation on top of the laser DC driving current. On the receiver side (blue block in Fig. 1(b)), the signal at the detector output passes through a 2.5 MHz Low-Pass filter (BLP-2.5+ from Mini-Circuits), used to cut-off frequency components higher than 10 times the first harmonic of the modulation signal. The resulting analog signal is then digitized by a variable threshold comparator and, finally, decoded in real-time by a second Arduino DUE board, which compares it with a pre-stored message. The received signal is recorded via a 2.5 Gs/s 4-channel digital oscilloscope (Tektronix MDO3024 200 MHz). The performance of the system is evaluated in terms of PER, a relevant metric to assess the quality of data-structured digital transmission channels [34–38]. The PER is calculated as the ratio between the number of received packets with at least one wrong bit and the total amount of sent packets. We send 62500 packets, chosen as the best compromise between a reasonable measurement time (order of minutes) and an acceptable target PER threshold for error-free communication, corresponding to PER = 1.6×10^{-5}. Indeed, assuming a uniform distribution of the erroneous bits on the received packets, the PER can be directly related to the bit error rate (BER) [39], as shown in Sec. 4. The resulting BER threshold, $\sim 3 \times 10^{-7}$, is much smaller than the one required for, e.g., a reliable internet connection after implementation of forward error correction (FEC) codes [40].

3. Overview of attenuation and noise regimes

During the design of FSOCS, it is important to correctly evaluate the link budget and to determine the noise contributions influencing the SNR (signal-to-noise ratio) [41]. In addition to the dynamical effects of noise related to the optical signal propagation (e.g., flaring, scintillation, turbulence [42,43]), the noise in a FSOCS is given by a combination of the intensity noise of the source and the detector background noise. Depending on the optical signal attenuation and on the type of communication (long or short-range, high or low visibility), the FSOCS can

Optics EXPRESS

operate in different noise scenarios. In this work, we aim at implementing two configurations of communication, corresponding to two realistic attenuation regimes: the high attenuation regime (HAR), dominated by propagation and attenuation losses, and the low attenuation regime (LAR), where the intensity noise floor of the laser source prevails on the background noise of detector. As shown in the following sections, for each regime a thorough noise analysis is carried out and the performance of the FSOCS are experimentally studied.

3.1. *Detector-limited noise floor in HAR*

As a first step, the quality of the transmission channel has been assessed in HAR conditions. This may be the case for a long-range outdoor FSO communication where the high attenuation due to absorption and/or scattering by molecules and aerosol particles may lead to a very large extinction of the propagating optical beam [44,45]. In this regime, the residual optical power impinging could be as low as few nW's, and we expect the main noise contribution to be given by the detector background noise, which can even exceed the intensity noise floor of the laser (Fig. 2(a)). To implement this regime, we attenuate the optical power incident onto the detector to obtain a noise floor that is limited by the detector background, so that the laser intensity noise lays below the detector background noise (red and blue trace, Fig. 2(a)). In this configuration only the peaks corresponding to the AM signal (green trace) emerge above the noise floor. For this test, we operate the laser nearby the threshold of the lasing process (driving current I = 642 mA) so that the relative modulation depth (MD), calculated as the ratio between the peak-to-peak amplitude and the DC component of the signal, can reach large values, as it is not limited by the maximum absolute current modulation achievable by our modulator (see Sec. 3). This configuration is the most significant configuration from a standard communication point of view, as it corresponds to a pristine OOK amplitude modulation scheme. Using larger laser currents, instead, would maintain the laser in a stable single-mode operation (well above the lasing threshold in both ON and OFF phases) during the whole transmission process. However, this would limit the relative MD value achievable by our system (and hence the SNR).

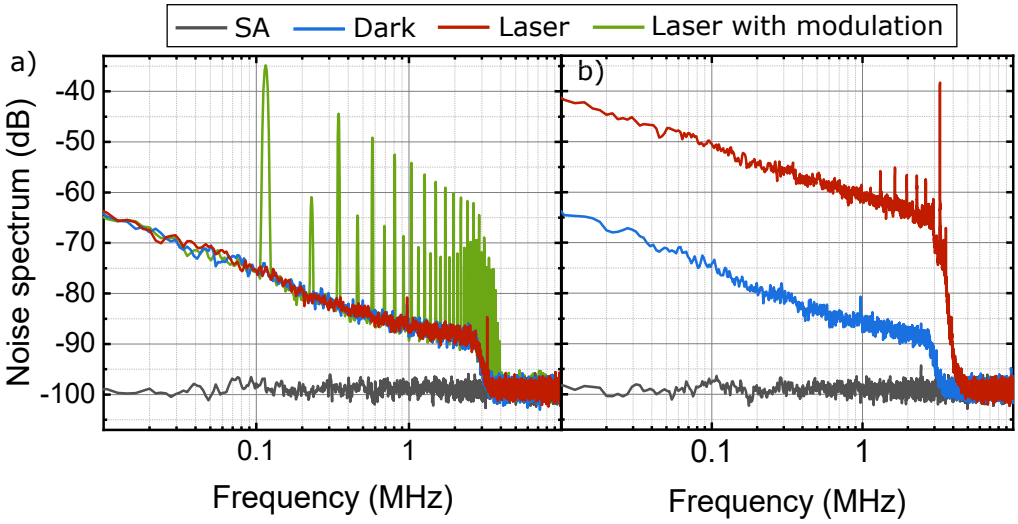

Fig. 2. Signal noise spectra in the HAR (a) and in the LAR (b). We show the recorded spectrum analyzer background (grey trace), the detector background (blue trace), the laser+detector without modulation (red trace) and applying a digital modulation at 115.2 kHz with a MD of 100% (green trace in (a)). In both graphs the frequency cutoff due to the 2.5 MHz low-pass filter is evident.

Optics EXPRESS

Even in HAR condition, where the FSOCS intensity noise floor is fully dominated by the detector background, we are able to detect the AC-modulated signal (green trace, Fig. 2(a)) which, after integration on the receiver bandwidth, corresponds to a SNR of 13 dB at the Manchester clock rate frequency of 115.2 kHz with a MD of 100%.

3.2. Source-limited noise floor in LAR

As a second step, we also explore the FSOCS application in the LAR (Fig. 2(b)). In this case, the amount of light collected by the RX stage is large enough that the intrinsic laser intensity noise contribution exceeds the background noise floor (red and blue trace, respectively, in Fig. 2(b)) and the background noise level of the RX stage is not expected to significantly affect the transmission quality. To explore this source-limited scenario, we set the laser current I = 662 mA (P_{out} = 12.9 mW) and we test the FSOCS for different MDs with a fixed optical attenuation of 14 dB. In this regime the laser is operated in a single-mode regime (above threshold), reducing intensity and frequency fluctuations due to small thermal instabilities. This regime could be relevant in FSOCSs with small channel losses, e.g., in good weather conditions, for short-range communication or/and in a controlled environment such as indoor FSO wireless communication. As shown in Fig. 2b, in these working conditions the detected noise floor lies well above the background noise (up to 20 dB) and it is dominated by the QCL intensity noise [46]. The QCL intensity noise spectrum features the typical $1/f$ trend of the flicker noise, characterizing this type of lasers [46–48].

4. Theoretical overview

4.1. Signal-to-noise ratio and packet error rate

The communication system performance can be characterized in terms of PER and SNR. For an OOK modulation, despite the noise spectrum of the system shows a global flicker noise shape (see Fig. 2(a)), due to the limited bandwidth over which the detection is performed, the noise can be safely approximated by an additive white Gaussian noise (AWGN) spectrum around the baseband frequency of 115.2 KHz. Under this assumption, the bit-error probability depends on the SNR through the well-known Q-function [49]: $\text{BER} = \text{Q}\left(\sqrt{\text{SNR}}\right)$. Assuming a uniform distribution of errors, the PER, in turn is connected to the BER through $\text{PER} = 1 - (1 - \text{BER})^{\text{N}} = 1 - \left(1 - Q\left(\sqrt{\text{SNR}}\right)\right)^{\text{N}}$ [39], where N is the number of the packet bits. Hence, PER can be related to the SNR. This latter parameter is related to the measured quantities via $\text{SNR(dB)} = 20\log\left(S_{\text{RX}}/2\sigma_{\text{RMS}}\right)$, where S_{RX} is the received peak-to-peak AC signal, and σ_{RMS} represents the root mean square (RMS) of the noise level. In order to relate our experimental investigation with realistic FSO communication conditions, where the commonly-used parameter is channel attenuation, we write the optical attenuation (OA) of the FSO channel as:

$$\text{OA(dB)} = -10\log\left(\frac{P_{\text{inc}}}{P_{\text{out}}}\right) = -10\log\left(\frac{S_{\text{RX}}}{G \cdot R \cdot MD \cdot P_{\text{out}}}\right), \tag{1}$$

where G = 26.5 is the gain of the AC transimpedance stage of the detector, R = 2793 V/W is the responsivity of the detector, and P_{out} is the optical power emitted by the QCL operating in single-mode. In particular, the factor $S_{\text{RX}}/(G \cdot R \cdot MD)$ is equal to the incident power onto the detector, P_{inc}. In order to characterize the performance of our FSOCS, we find convenient to define the maximal optical attenuation (MOA) as the largest tolerable channel attenuation to attain a defined threshold PER value. In quantifying the MOA we consider optical power as the maximum yet guaranteeing stable single-mode operation of the QCL (P_{max} = 21 mW). It is possible to estimate the MOA by replacing P_{out} with P_{max} in Eq. (1). In the LAR regime we study the PER for different MD values, each labeled by the index i. Fixing P_{max}, G and R gives

Optics EXPRESS

a constant ratio $S_{RX}/\sigma_{\mathrm{RMS}} = k_i$, since both the terms are proportional to the residual optical power collected by the RX stage after the optical attenuation stage. In the HAR regime we study the PER as the MOA varies. Therefore, it is useful to rewrite the SNR as a function of MOA, considering $P_{\mathrm{out}} = P_{\mathrm{max}}$. This yields the following set of relations:

$$\mathrm{SNR}_i(\mathrm{dB}) = \begin{cases} k_{\mathrm{i}} & \text{in LAR,} \\ D_i(\mathrm{dB}) - 2\ \mathrm{MOA(dB)} & \text{in HAR,} \end{cases} \tag{2}$$

where $D_{\mathrm{i}} = 20 \log\left(\dfrac{G \cdot R \cdot MD \cdot P_{\mathrm{max}}}{2\sigma_{\mathrm{RMS}}}\right)$ is constant in our measurement conditions, and represents the SNR_{i} for negligible channel attenuation.

4.2. Modeling outdoor FSO links

In order to relate the retrieved data to realistic outdoor FSO communication scenarios, it is necessary to model and simulate common outdoor conditions in terms of experimentally accessible parameters. In an outdoor FSO link, the propagating beam is attenuated by atmospheric factors such as particle scattering (e.g., by molecules, aerosols, dust, smoke), molecular absorption, and weather conditions (rain, mist, snow, and fog) [45]. In addition, the quality of the received signal can be also affected by geometrical factors such as beam divergence [45]. Regarding the atmospheric attenuation, we simulate a simplified scenario that considers particle scattering (i.e., molecules, aerosol), absorption, and scintillation due to turbulence (Fig. 3). In these conditions, the atmospheric attenuation coefficient due to scattering and absorption is described as [41]: $\gamma(\lambda) = \alpha_{\mathrm{m}}(\lambda) + \alpha_a(\lambda) + \beta_{\mathrm{m}}(\lambda) + \beta_{\mathrm{a}}(\lambda)$, where λ is the laser wavelength, $\alpha_{\mathrm{m}}(\lambda)$ and $\alpha_{\mathrm{a}}(\lambda)$ are the molecular (m) and aerosol (a) absorption coefficients, respectively, while $\beta_{\mathrm{m}}(\lambda)$ and $\beta_{\mathrm{a}}(\lambda)$ are the scattering ones. It is difficult to give a precise *a priori* estimation of absorption coefficients, as they depend on the gaseous composition of the air, which can vary consistently with the specific scenario. For instance, the composition varies at different altitudes and/or latitudes, as well as for different seasons and environments (e.g., countryside, city, desert, sea). In our work, we estimate the absorption coefficient by using the atmospheric model named *USA model, mean latitude, summer,* $H = 0$ of the HITRAN database [50–52], where $H = 0$ is the altitude (sea level). In the simulation, we consider both Rayleigh and Mie scattering types. The former describes the scattering due to particles with a radius $r << \lambda$ (e.g., molecules). The latter describes the scattering due to aerosol (like fog, clouds, and haze) where $r \simeq \lambda$ [41]. We use the formula of the LOWTRAN code for the Rayleigh scattering attenuation due to molecules [53]. The attenuation coefficient $\beta_{\mathrm{a}}(\lambda)$ due to aerosol is calculated as a function of the visibility V (expressed in km), where V is defined as the distance at which the optical power of a propagating beam of visible green light ($\lambda_0 = 550$ nm) decreases down to 2% of its original value [43]. The formula we adopted is the empirical one typically applied in case of fog [41–43]:

$$\beta_{\mathrm{a}}(\lambda) = 10 \log(\mathrm{e}) \frac{3.91}{V} \left(\frac{\lambda}{\lambda_0}\right)^{-p} \tag{3}$$

$$\text{with} \quad p = \begin{cases} 1.6 & V > 50\ \mathrm{km} \\ 1.3 & 6\ \mathrm{km} < V < 50\ \mathrm{km} \\ 0.585 V^{\frac{1}{3}} & V < 6\ \mathrm{km} \end{cases} \tag{4}$$

where λ is expressed in nm, and p is a coefficient related to the size distribution of the scattering particles, according to the Kruse model [41]. Starting from this empirical formula, it is possible to evaluate the attenuation due to weather conditions in several cases such as heavy fog, light haze/drizzle and clear sky [41]. In case of intense rain or snow, which are outside the purpose of this work, other formulas must be considered [42,43].

Optics EXPRESS

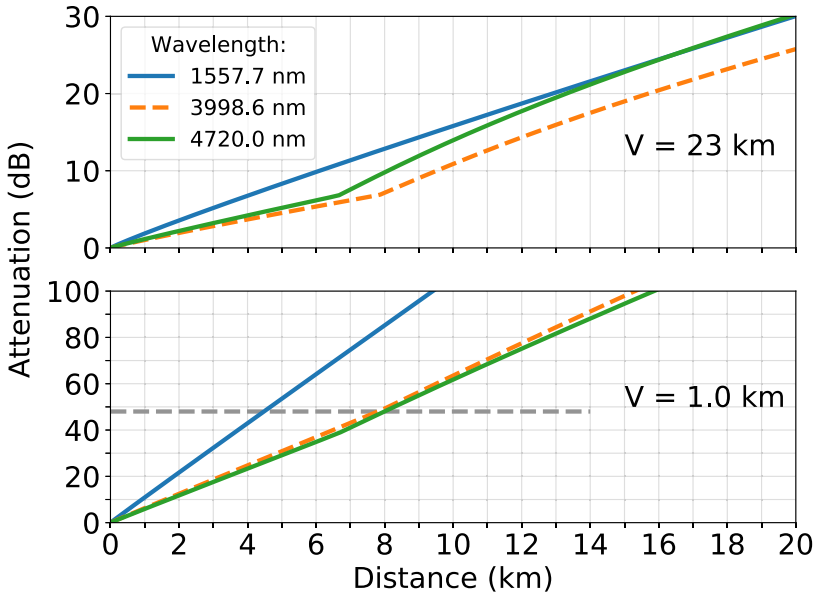

Fig. 3. Simulation of the attenuation as a function of the communication distance for a terrestrial point-to-point FSO communication at sea level, for very clear-air condition (V = 23 km (upper graph)), and adverse weather conditions (V = 1 km (lower graph)). In the graphs, the attenuation due to scattering, atmospheric absorption (HITRAN database [50–52]), beam divergence (geometrical attenuation) and scintillation are considered. We assume to have both a receiver and a transmitter with an optical aperture radius of 10 cm, and that the geometrical losses start affecting the signal after twice the Rayleigh length. The dashed gray line represents the error-free communication limit characterizing our system.

The effect of turbulence, $A_{\text{sci}}(dB)$ can be taken into account by using the formula [54,55]:

$$A_{\text{sci}}(\text{dB}) = 2 \cdot \sqrt{23.17 \cdot k^{7/6} \cdot C_{\text{n}}^2 \cdot L^{11/6}} \tag{5}$$

that describes the losses due to scintillation, where $k = 2\pi/\lambda$ is the wavenumber, L is the link range in meters and C_{n}^2 is the refractive index structure parameter in $\text{m}^{2/3}$ calculated via the Hufnagel-Valley model [56]. A wind speed of 30 km/h and a quote of 50 m over the sea level are considered to retrieve the C_{n}^2 factor in the typical case of moderate turbulence condition [54]. Our simulation also accounts for the geometrical attenuation factor due to the Gaussian propagation of the laser beam, leading to a divergence in the far-field region. The geometrical attenuation results in a $1/d^2$ scaling of the far-field intensity impinging on the detector, where d represents the TX-RX distance. Furthermore, it depends on the laser wavelength and on the optical aperture of the light-collecting system at the receiver side [42,43]. In this work, we simulate a system where the radius of both the transmitter and the receiver aperture is 10 cm. We estimate the geometrical attenuation coefficient A_{geo} via the following equation [42,43]:

$$A_{\text{geo}}(dB) = \begin{cases} 10 \log\left(\dfrac{S_{\text{d}}}{S_{\text{capture}}}\right) & S_{\text{d}} > S_{\text{capture}}, \\ 0 & \text{otherwise}, \end{cases} \tag{6}$$

where S_{d} is the wavefront area of the transmitted beam at the receiver at a distance d, and S_{capture} is the receiver capture surface. Within short distances it is possible that S_{capture} is larger than the beam area. In this case, all the light is collected and $A_{\text{geo}}(dB)$ is equal to zero [42,43]. For sake

Optics EXPRESS

of simplicity, in our model we assume this to happen for distances lower than twice the Rayleigh length, where we assume no geometrical losses. For longer distances we evaluate the losses considering a receiver aperture smaller than the diameter of the diverging beam. In Fig. 3, we show the combined atmospheric and the geometrical attenuation coefficients for two different values of visibility V, making a comparison between the wavelength used in this experiment (λ = 4720.0 nm), with the optimal mid-IR wavelength for air transmission (λ = 3998.6 nm) and the optimal telecom one (λ = 1557.7 nm). The total attenuation A_{all}(dB) reported in figure is calculated as $A_{\mathrm{all}}(\mathrm{dB}) = A_{\mathrm{geo}}(\mathrm{dB}) + A_{\mathrm{sci}}(\mathrm{dB}) + \gamma(\mathrm{dB})$, with γ(dB) is $\gamma(\lambda)$ expressed in dB. In particular, the optimal mid-IR wavelength around 4 µm features the lowest absorption as a result of a thorough high-resolution analysis of the atmospheric absorption spectrum provided by the HITRAN database [50]. Assuming the same setup geometry, the impact of geometrical attenuation is in general greater in the mid-IR than in the NIR due to the larger wavelength. On the other hand, scintillation effects impact more on the telecom wavelengths. In the case of very clear air condition, corresponding to V = 23 km [41,42], the top plot in Fig. 3 shows that the optimal mid-IR wavelength (orange dashed curve) is less attenuated than the other wavelengths in all the distance range took into account. Over short distances, below 10 km, the used wavelength (green curve) is still convenient over the NIR one (blue curve), while for longer distances the two wavelengths perform similarly. On the other hand, the lower graph shows the expected optical channel attenuation as a function of distance in case of low visibility, V = 1 km, corresponding to heavy fog and cloud [41], which is dominated by scattering. Remarkably, in this case of low visibility, the mid-IR wavelengths are in general much less affected by the losses than NIR ones, and the optimal system at 4.0 µm [30] shows an advantage of 4–5 dB over the whole explored distance range of 20 km for low visibility. Interestingly, however, Fig. 3 also highlights that in the atmospheric conditions set for the simulation (moderate turbulence), the optimal mid-IR systems outperforms the standard telecom one also in the large visibility condition, due to an optimal combination of geometrical propagation and reduced scattering properties.

5. Experimental results and discussion

As anticipated in Sec. 4, in the following Section we characterize the system performance in terms of PER and SNR recorded in both HAR and LAR configurations.

Our measurements will then be combined with the predictions of the channel model discussed in Sec. 4. to give an estimation of the maximum mid-IR link length attainable with our system in various realistic visibility conditions.

5.1. High attenuation regime (HAR)

In the HAR we aim at determining the system response as a function of channel attenuation, and to give an estimation of the MOA tolerable by our QCL-based mid-IR communication system for granting reliable optical links given a requested PER value. In Fig. 4(a), we first show the dependence of the measured PER on the SNR, considering the recorded value of σ_{RMS} = 2.3 mV given by the detector background noise. The error bars on PER are obtained as the standard deviation on repeated measurements, while the SNR error bars are obtained after error propagation from measurements of σ_{RMS} and S_{Rx} values. The red curve represents the PER model as a function of SNR (see Sec. 4), fixing σ_{RMS} at 2.3 mV. It is in good agreement with data. The error-free communication (PER $< 1.6 \times 10^{-5}$) is achieved for a SNR larger than 14 dB. Figure 4 also shows the recorded eye patterns in low-signal (SNR = 6 dB, PER ~ 0.5, (b)), medium-signal (SNR = 10 dB, PER ~ 0.02, (c)), and high-signal (SNR = 13.5 dB, error-free, (d)) configurations. The traces report the self-triggered signal after the amplified photodetector RX stage. The jitter observed on the transition edges of the eye pattern depends on the signal quality and its value is related to the intrinsic time resolution of the Arduino DUE TX board (~ 1 µs). Figure 4 reports the observed MOA as a function of PER, for MD=100%.

Optics EXPRESS

An error-free communication is achieved for MOA lower than 48 dB. Assuming an internet connection reference value of PER = 10^{-3}, the relative observed MOA is slightly higher (49.5 dB). The error bars on MOA are calculated with the propagation of the statistical errors obtained during signal and noise acquisitions. The shaded stripe in Fig. 4 is a guide to the eyes and suggests that the MOA increases by 2 dB every 3 decades of PER (for PER<1). This behaviour agrees with the expected theoretical trend described in Sec. 4. For example, let's consider two different values of MOA=48.5 dB and MOA=50.5 dB for MD = 100%. The relative values of SNR(dB) obtained from (2) are SNR = 13 dB (MOA=48.5 dB) and SNR = 9 dB (MOA=50.5 dB). By converting these values in linear scale, through the relations reported in Sec. 4) we can obtain the relative PERs values. In agreement with our observations, these differ by 3 decades for the two selected values of MOA, approximately.

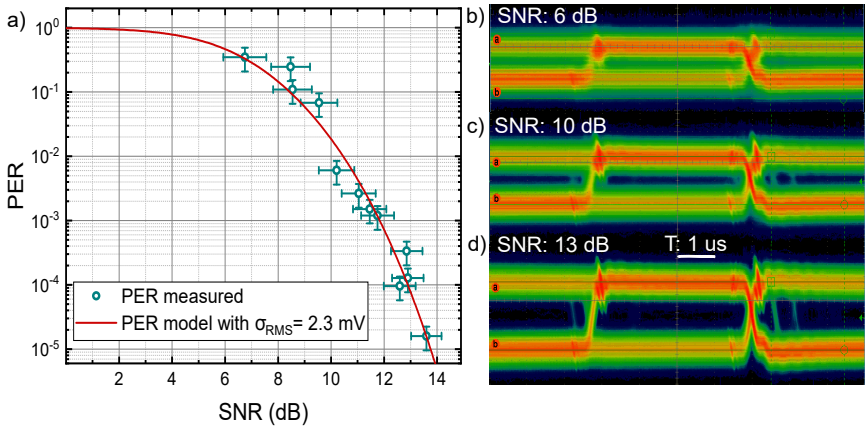

Fig. 4. (a) PER as a function of the SNR in the HAR. Measured data points (green circles) feature a very nice agreement with predictions of the PER model for a $\sigma_{\mathrm{RMS}} = 2.3$ mV, which corresponds to the measured RMS. The error-free communication threshold of 1.6×10^{-5} is achieved for SNR > 14 dB. The vertical error bars orrespond to the standard deviation after repeated measurements, while horizontal error bars are obtained after error propagation from measurements of σ_{RMS} and S_{RX} values. (b)–(d) Eye patterns for three different values of SNR (6 , 10 , 13 dB respectively) corresponding to three different PER regimes. The horizontal scale is 1 µs/ div, while the vertical scale is 10 mV/ div. The acquisition is self triggered on the received signal.

5.2. *Low attenuation regime (LAR)*

In the LAR, both noise and signal amplitude are expected to grow linearly with P_{out}. In contrast, however, SNR is still expected to grow with MD. In particular, for MDs much lower than 100%, we expect SNR $\propto$ MD. For this reason, we investigate the minimum MD (in the low-modulation regime) needed for an error-free communication for given values of OA in the optical link. By identifying the minimum required modulation, we can define the best working condition for the setup in terms of laser stability and spectral quality. This is a relevant issue when, e.g., more sophisticated modulation schemes (such as OFDM) aimed at larger bit-rates are involved, where both amplitude and frequency stability of the baseband signal are critical factors. In such cases, a strict single-mode operation of the laser source is essential. As in the case of HAR, we first evaluate the communication performance against the recorded SNR (Fig. 6). In this case, the PER model curve which most accurately describes the measured values (green circles) is obtained by choosing a $\sigma_{\mathrm{RMS}} = 40$ mV (red curve). This σ_{RMS} value slightly differs from the measured RMS noise value $\sigma_{\mathrm{RMS}} = 32$ mV (blue dashed line), which we measure when no transmission

Optics EXPRESS

occurs. This slight underestimation of noise value could be addressed to the presence of fast transients and glitches that can occur during the transmission, as a consequence of irradiated EM noise due to the large and steep variations of current levels involved in the modulation process. We note that in the HAR this effect is negligible, as the predominant noise contribution is related to the background noise of the detector. Figure 6 also shows the eye patterns for three different MDs (0.3 % (b), 0.6 % (c), and 1.3 % (d)) corresponding to low, medium and high SNR (SNR=9 dB with a PER ~ 0.2, SNR=13 dB with PER ~ 0.003, and SNR>16 dB with PER$\lesssim 10^{-5}$, respectively). As introduced in Sec. 4, in case of LAR we experimentally evaluate the communication performance of our FSOCS for different MDs, to find the minimum MD required to perform an error-free communication for a given value of P_{out}. We remark that in this regime, where the detection noise is dominated by the intrinsic intensity noise of the source, we do not expect significant improvement in the communication quality by increasing the optical power emitted by the QCL source. The SNR(dB) linearly improves with the MD as described by Eq. (2) and, with reference to Fig. 7, an error-free communication is obtained for MDs greater than 1%. The error bars are calculated as in the HAR case.

5.3. HAR-LAR transition

The versatility of our FSOCS, along with the testing facility, allowed us to investigate the behaviour of the system in the transition between HAR and LAR, i.e., between the noise regimes described in Sec.3. In particular, we vary the attenuation of the optical link from 15 dB to 32 dB for three different MDs (0.5%, 0.7%, and 1%), as shown in Fig. 8. Even in this case the laser operates in single-mode regime well above threshold (I = 663 mA, P_{out} = 13.6 mW).

Figure 8(a) reports the observed SNR as a function of the MOA. Our observations clearly confirm the existence of two distinct noise regimes depending on the global attenuation affecting the optical channel. For low attenuations (LAR), where the detection noise is dominated by the QCL intensity noise, SNR does not significantly depend on the optical signal impinging on the RX stage. In contrast, for MOA larger than a critical value (25 dB in our case) the SNR decreases as the attenuation grows (HAR). The shaded areas, intended as a guide to the eye, highlight a SNR vs MOA decrease ratio of ~ 2 dB/dB, which is compatible with predictions of Eq. (2) in the HAR regime. In the LAR, the constant value of the SNR (given by k_i in Eq. (2)), depends on the MD, as this influences the effective amplitude of AC signal recorded by the RX stage. The reduction in the (constant) SNR values recorded in LAR for different MDs are in good agreement with the expectations yielded by Eq. (2). For example, with reference to Fig. 8(a), a reduction of 50% in the MD results in an effective reduction of −6 dB in the observed SNR, as a comparison between green and red data points confirms. The observed behaviour is reflected into the communication performance, where a steep increase in the recorded PER is observed above the 25 dB transition point (HAR). Conversely, in agreement with what has been observed for the SNR values, in the LAR the system is featuring stable communication performance independently on the channel attenuation, as the main noise source in the detection stage is represented by the intrinsic intensity noise of the QCL source.

5.4. Estimation of the outdoor performance of the FSO links

We now relate our experimental findings on our mid-IR FSOCS to possible realistic scenarios. In particular, we are interested in estimating the maximum effective length of an FSO link employing our communication system under adverse atmospheric conditions, where mid-IR links are expected to outperform NIR ones. We remark that whilst such estimation does not exactly correspond to real FSO link lengths as scintillation is the only turbulence phenomenon accounted for by our model, such estimation still provides very realistic insights on the potential cast of our mid-IR FSOCS as compared to other systems in real conditions. To obtain the effective link lengths, we consider the case of large attenuation (HAR) and maximal MD (100%). We can

Optics EXPRESS

combine our experimental results on MOA in HAR (Fig. 5) with the expected channel attenuation given by the model predictions (Fig. 3). According to Fig. 5, an error-free communication (PER$<1.6 \times 10^{-5}$) requires MOA < 48 dB. A comparison with Fig. 3, allows us to obtain the error-free communication distance in both high- and low- visibility cases ($V = 1$ km and $V = 23$ km), and for the three values of wavelength discussed in Sec. 4. and Sec. 3. (i.e., a telecom NIR source ($\lambda \sim 1.56\,\mu$m), our mid-IR source ($\lambda \sim 4.72\,\mu$m), and the optimal mid-IR wavelength ($\lambda \sim 4.0\,\mu$m) which would minimize the effects of atmospheric absorption and scattering).

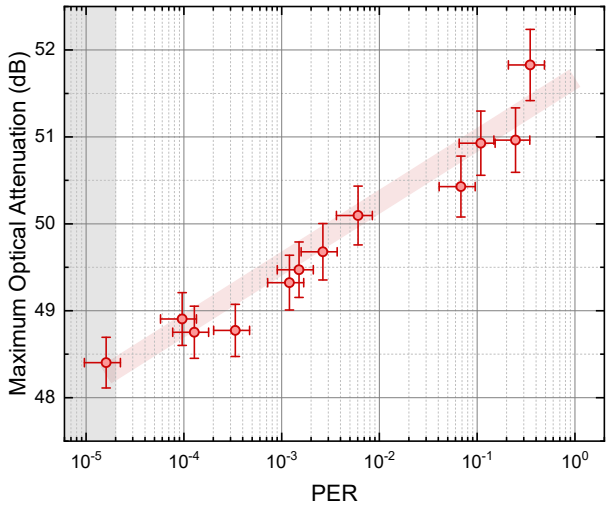

Fig. 5. MOA as a function of the PER for MD=100% in the HAR. The gray shaded area highlights the threshold for an error-free communication, it is achieved for MOA lower than 48 dB. The oblique shaded stripe is a guide to the eye, to highlight the trend of MOA. MOA increases by 2 dB every 3 decades of PER.

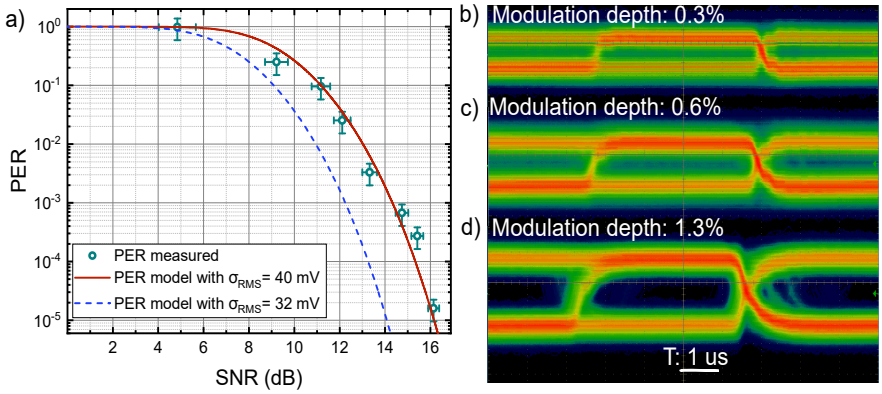

Fig. 6. (a) Communication performance as a function of the SNR in the LAR. The green circles represent the measured PER, while the dashed blue curve and the red solid curve correspond to the simulated PER with $\sigma_{\mathrm{RMS}} = 32$ mV (experimental value) and $\sigma_{\mathrm{RMS}} = 40$ mV (best agreement value), respectively. (b)–(d) Eye patterns for three different MDs: 0.3% (corresponding to PER $\sim$ 0.2); 0.6% (corresponding to PER $\sim$ 0.003); 1.3% (error-free communication).

Optics EXPRESS

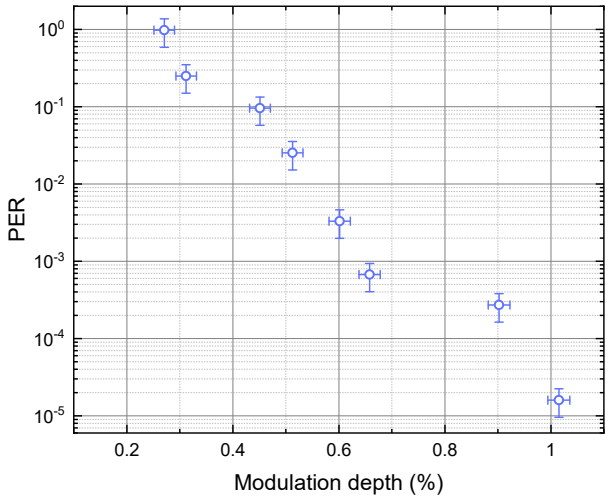

Fig. 7. PER as a function of the MD in the LAR, for a fixed OA of 14 dB. The error-free communication is established for MDs greater than 1%.

Table 1 reports the expected maximum link lengths estimated through such analysis. In the low-visibility case, our mid-IR prototype at 4.72 µm is expected to grant error-free communication for link lengths up to 8.0 km, larger than the attainable distance of 4.5 km estimated for the standard NIR telecom source at 1.56 µm. The performance at 4.0 µm wavelength is comparable to the one at 4.72 µm. This effect is mostly due to the reduced scattering effects, which are larger for short wavelengths (Eq. (3)), confirming the extreme relevance of mid-IR FSO links as valid alternative to NIR telecom systems in case of adverse atmospheric conditions. We remark that the 4.0 µm range is at full reach of actual mid-IR QCL chips, making QCLs one of the most versatile platform for optimal FSOCS to be employed in realistic applications.

Table 1. Estimated effective link lengths for an error-free communication in low-visibility conditions (V = 1 km) for a conventional telecom source (λ = 1.56 µm), and for two different mid-IR sources (the one used in this experiment at 4.72 µm and one with the optimal transmission wavelength around 4.0 µm). We consider a MD=100% and HAR configuration.

	NIR source (λ = 1.56 µm)	**mid-IR source** (λ = 4.72 µm)	**mid-IR source** (λ = 4.0 µm)
V = 1 km	< 4.5 km	< 8.0 km	< 7.8 km

Optics EXPRESS

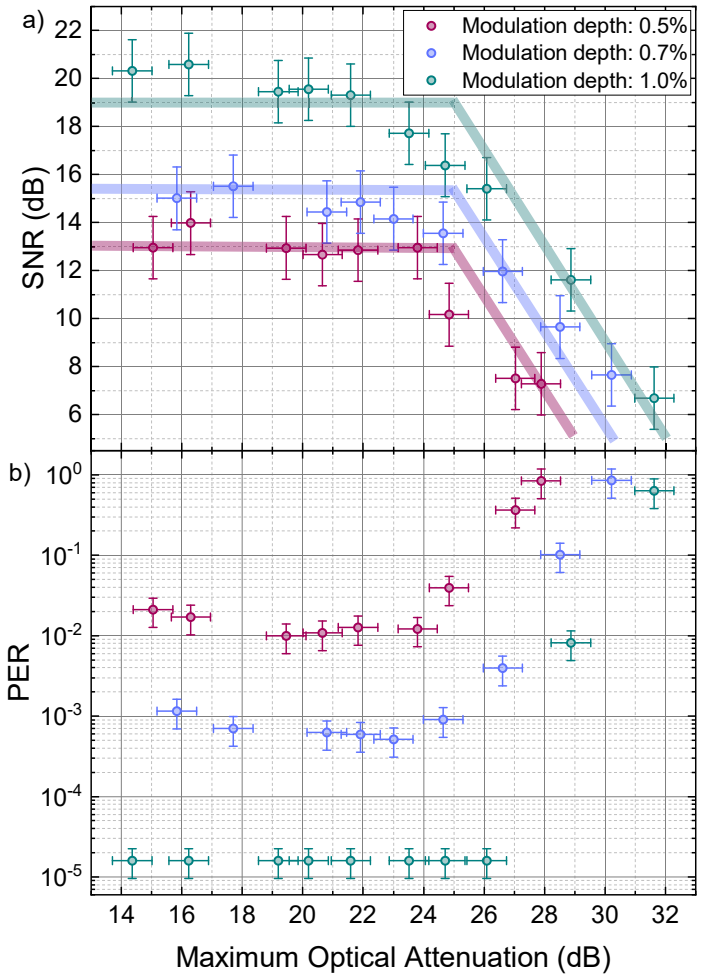

Fig. 8. (a) SNR as a function of the MOA for three different MDs, 0.5% (purple dots), 0.7% (light blue dots) and 1% (green dots). For MOA up to ~ 25 dB, the system is limited by the QCL noise, which increases as the signal, therefore the SNR remains constant (shaded areas, which are only a guide to the eye). For greater attenuation, the system is limited by the detector noise floor and the SNR approximately decreases by 2 dB/dB (slanting lines). (b) PER as a function of MOA across the HAR-LAR transition region. The PER shows a plateau for low MOA values, and increases for larger MOAs, as suggested by Eq. (2).

Optics EXPRESS

6. Conclusions

In this work, we have presented for the first time an extensive characterization of noise regimes that could occur in QCL-based FSOCS, based on a versatile mid-IR QCL system at 4.72 µm. We carried out a detailed study of communication performances in two different noise regimes (HAR and LAR), finding a very different response of the system in terms of transmission quality as a function of the optical channel attenuation. In the HAR, where the predominant noise contribution is given by the detector noise, the system communication is tested against the maximal optical attenuation tolerable in order to achieve error-free communication (PER$<1.6 \times 10^{-5}$), finding MOA values as high as 48 dB for 100% modulation depths and a baudrate of 115 kbaud. In contrast, in the LAR regime, which is more typical of short-range links, we observed an almost constant PER as a function of the optical attenuation, as a consequence of a SNR value which is independent of the received signal amplitude S_{RX}. The versatility of our setup also allowed us to characterize the transition region between the HAR and LAR regimes, in terms of both SNR and tolerable MOA, finding a clear crossing point between the two regimes. We also estimate the performance of our mid-IR FSOCS under realistic operational conditions by combining our findings with the predictions of a simplified propagation model taking into account both geometrical and atmospheric (absorption, scattering, and scintillation) effects for moderate turbulence, comparing them with the performance expected for different NIR and mid-IR wavelengths. The estimated error-free link length for the presented mid-IR FSOCS is 8.0 km in low visibility conditions (V = 1 km). Noticeably enough, in such a low visibility condition, this overwhelms the expected performance for a standard source in the telecom range which, in contrast, is favored by a lower divergence in the far field due to the shorter wavelength. However, our analysis shows that a FSOCS based on mid-IR QCLs at an optimal wavelength of 4.0 µm [30] could also overperform NIR systems in good visibility, simultaneously featuring excellent resilience to scattering and good propagation properties.

The results presented in this work have a general breadth, and could have a deep impact for future QCL-based FSOCs, also working in different wavelength regions and featuring Gbps-class bitrates.

Funding. H2020 Future and Emerging Technologies (Qombs Project, 820419, QuaLIDAD Project, 101034794); Ministero dell'Istruzione, dell'Università e della Ricerca (FOE Progetto Premiale 2015 "OpenLab 2", PON 2017 ARS01_00917 "OK-INSAID"); Laserlab-Europe (871124); Italian ESFRI Roadmap (Extreme Light Infrastructure - ELI Project); Consiglio Nazionale delle Ricerche (Progetti di Ricerca @CNR, "TEROCODE" and "FluoCom" projects).

Acknowledgments. The Authors gratefully thank the collaborators within the consortium of the Qombs Project: Prof. Dr. Jérome Faist (ETH Zurich) for having provided the quantum cascade laser and the company ppqSense for having provided the ultra-low-noise current driver (QubeCL). In addition, the Authors gratefully thank all the members of the VisiCore joint laboratory for Research on Visible Light Communications.

Disclosures. The authors declare no conflicts of interest.

Data availability. Data underlying the results presented in this paper are not publicly available at this time but may be obtained from the authors upon reasonable request.

References

1. H. Willebrand and B. Ghuman, "Fiber optics without fiber," IEEE Spectrum **38**(8), 40–45 (2001).
2. M. A. Esmail, A. M. Ragheb, H. A. Fathallah, M. Altamimi, and S. A. Alshebeili, "5g-28 ghz signal transmission over hybrid all-optical fso/rf link in dusty weather conditions," IEEE Access **7**, 24404–24410 (2019).
3. D. Marabissi, L. Mucchi, S. Caputo, F. Nizzi, T. Pecorella, R. Fantacci, T. Nawaz, M. Seminara, and J. Catani, "Experimental measurements of a joint 5g-vlc communication for future vehicular networks," J. Sens. Actuator Networks **9**(3), 32 (2020).
4. K. David and H. Berndt, "6G vision and requirements: Is there any need for beyond 5G," IEEE Veh. Technol. Mag. **13**(3), 72–80 (2018).
5. S. Dang, O. Amin, B. Shihada, and M.-S. Alouini, "What should 6g be," Nat. Electron. **3**(1), 20–29 (2020).
6. M. Dehghani Soltani, E. Sarbazi, N. Bamiedakis, P. de Souza, H. Kazemi, R. V. Penty, H. Haas, and M. Safari, "Safety analysis for laser-based optical wireless communications: A tutorial," arXiv:2102.08707 (2021).

Optics EXPRESS

7. M. T. A. Khan, M. A. Shemis, E. Alkhazraji, A. M. Ragheb, M. A. Esmail, H. Fathallah, S. Alshebeili, and M. Z. M. Khan, "Optical wireless communication at 100 Gb/s using l-band quantum-dash laser," in *Conference on Lasers and Electro-Optics Pacific Rim (CLEO-PR)* (2017), pp. 1–3.
8. S. Bloom, E. Korevaar, J. Schuster, and H. Willebrand, "Understanding the performance of free-space optics *invited*," J. Opt. Netw. **2**(6), 178–200 (2003).
9. J. Faist, F. Capasso, D. L. Sivco, C. Sirtori, A. L. Hutchinson, and A. Y. Cho, "Quantum cascade laser," Science **264**(5158), 553–556 (1994).
10. Y. Su, W. Wang, X. Hu, H. Hu, X. Huang, Y. Wang, J. Si, X. Xie, B. Han, H. Feng, Q. Hao, G. Zhu, T. Duan, and W. Zhao, "10 Gbps DPSK transmission over free-space link in the mid-infrared," Opt. Express **26**(26), 34515–34528 (2018).
11. P. Corrigan, R. Martini, E. A. Whittaker, and C. Bethea, "Quantum cascade lasers and the kruse model in free space optical communication," Opt. Express **17**(6), 4355–4359 (2009).
12. L. Flannigan, L. Yoell, and C. Q. Xu, "Mid-wave and long-wave infrared transmitters and detectors for optical satellite communications—a review," J. Opt. **24**(4), 043002 (2022).
13. G. Xu, "Error performance of deep space optical communication with m-ary pulse position modulation over coronal turbulence channels," Opt. Express **27**(9), 13344–13356 (2019).
14. L. Tombez, F. Cappelli, S. Schilt, G. Di Domenico, S. Bartalini, and D. Hofstetter, "Wavelength tuning and thermal dynamics of continuous-wave mid-infrared distributed feedback quantum cascade lasers," Appl. Phys. Lett. **103**(3), 031111 (2013).
15. J. Faist, *Quantum Cascade Lasers* (Oxford University Press, 2013).
16. S. Riedi, F. Cappelli, S. Blaser, P. Baroni, A. Müller, and J. Faist, "Broadband superluminescence, 5.9μm to 7.2μm, of a quantum cascade gain device," Opt. Express **23**(6), 7184–7189 (2015).
17. O. Cathabard, R. Teissier, J. Devenson, J. Moreno, and A. Baranov, "Quantum cascade lasers emitting near 2.6 μm," Appl. Phys. Lett. **96**(14), 141110 (2010).
18. R. Paiella, R. Martini, F. Capasso, C. Gmachl, H. Y. Hwang, D. L. Sivco, J. N. Baillargeon, A. Y. Cho, E. A. Whittaker, and H. Liu, "High-frequency modulation without the relaxation oscillation resonance in quantum cascade lasers," Appl. Phys. Lett. **79**(16), 2526–2528 (2001).
19. B. Hinkov, A. Hugi, M. Beck, and J. Faist, "Rf-modulation of mid-infrared distributed feedback quantum cascade lasers," Opt. Express **24**(4), 3294–3312 (2016).
20. L. Consolino, F. Cappelli, M. Siciliani de Cumis, and P. De Natale, "QCL-based frequency metrology from the mid-infrared to the THz range: a review," Nanophotonics **8**(2), 181–204 (2018).
21. S. Borri, G. Insero, G. Santambrogio, D. Mazzotti, F. Cappelli, I. Galli, G. Galzerano, M. Marangoni, P. Laporta, V. Di Sarno, L. Santamaria, P. Maddaloni, and P. De Natale, "High-precision molecular spectroscopy in the mid-infrared using quantum cascade lasers," Appl. Phys. B **125**(1), 18 (2019).
22. M. Gutowska, D. Pierścińska, M. Nowakowski, K. Pierciński, D. Szabra, J. Mikołajczyk, J. Wojtas, and Z. Bielecki, "Transmitter with quantum cascade laser for free space optics communication system," Bull. Pol. Acad. Sci. Tech. Sci. **59**(4), 419–423 (2011).
23. J. Mikołajczyk, "An overview of free space optics with quantum cascade lasers," Int. J. Electron. Telecommun. **60**(3), 259–264 (2014).
24. C. Liu, S. Zhai, J. Zhang, Y. Zhou, Z. Jia, F. Liu, and Z. Wang, "Free-space communication based on quantum cascade laser," J. Semicond. **36**(9), 094009 (2015).
25. N. Corrias, T. Gabbrielli, P. De Natale, L. Consolino, and F. Cappelli, "Analog FM free-space optical communication based on a mid-infrared quantum cascade laser frequency comb," Opt. Express **30**(7), 10217–10228 (2022).
26. O. Spitz, P. Didier, L. Durupt, D. A. Díaz-Thomas, A. N. Baranov, L. Cerutti, and F. Grillot, "Free-space communication with directly modulated mid-infrared quantum cascade devices," IEEE J. Sel. Top. Quantum Electron. **28**(1: Semiconductor Lasers), 1–9 (2022).
27. X. Pang, O. Ozolins, L. Zhang, R. Schatz, A. Udalcovs, X. Yu, G. Jacobsen, S. Popov, J. Chen, and S. Lourdudoss, "Free-space communications enabled by quantum cascade lasers," Phys. Status Solidi A **218**(3), 2000407 (2021).
28. X. Pang, R. Schatz, M. Joharifar, A. Udalcovs, V. Bobrovs, L. Zhang, X. Yu, Y.-T. Sun, G. Maisons, M. Carras, S. Popov, S. Lourdudoss, and O. Ozolins, "Direct modulation and free-space transmissions of up to 6 gbps multilevel signals with a 4.65- μm quantum cascade laser at room temperature," J. Lightwave Technol. **40**(8), 2370–2377 (2022).
29. H. Dely, T. Bonazzi, O. Spitz, E. Rodriguez, D. Gacemi, Y. Todorov, K. Pantzas, G. Beaudoin, I. Sagnes, L. Li, A. G. Davies, E. H. Linfield, F. Grillot, A. Vasanelli, and C. Sirtori, "10 gbit s-1 free space data transmission at 9 μm wavelength with unipolar quantum optoelectronics," Laser Photonics Rev. **16**(2), 2100414 (2022).
30. C. Sauvage, C. Robert, B. Sorrente, F. Grillot, and D. Erasme, "Study of short and mid-infrared telecom links performance for different climatic conditions," Proc. SPIE **11153**, 111530I (2019).
31. 14 dB is the minimum value of attenuation black required when the laser operates well above threshold with P_{out} = 12.9mW to prevent the detector saturation and its degradation. This is the power working regime that we use to investigate the LAR for different values of MD. 52 dB is the maximum value of attenuation applicable black to detect the modulation signal with the laser operating nearby threshold at I = 642mA and P_{out} = 1.66mW. These are the working conditions selected to test our FSOCS in case of HAR and MD=100%.
32. T. Gabbrielli, F. Cappelli, N. Bruno, N. Corrias, S. Borri, P. D. Natale, and A. Zavatta, "Mid-infrared homodyne balanced detector for quantum light characterization," Opt. Express **29**(10), 14536–14547 (2021).

Optics EXPRESS

33. S. Rajagopal, R. D. Roberts, and S.-K. Lim, "IEEE 802.15.7 visible light communication: modulation schemes and dimming support," IEEE Commun. Mag. **50**(3), 72–82 (2012).
34. M. Seminara, T. Nawaz, S. Caputo, L. Mucchi, and J. Catani, "Characterization of Field of View in Visible Light Communication Systems for Intelligent Transportation Systems," IEEE Photonics J. **12**(4), 1–16 (2020).
35. P. Ashok and M. Ganesh Madhan, "Performance analysis of various pulse modulation schemes for a fso link employing gain switched quantum cascade lasers," Opt. Laser Technol. **111**, 358–371 (2019).
36. A. Malik and P. Singh, "Free space optics: Current applications and future challenges," Int. J. Opt. **2015**, 1–7 (2015).
37. A. K. Majumdar, *Optical Wireless Communications for Broadband Global Internet Connectivity* (Elsevier, 2019).
38. M. Meucci, M. Seminara, T. Nawaz, S. Caputo, L. Mucchi, and J. Catani, "Bidirectional vehicle-to-vehicle communication system based on VLC: Outdoor tests and performance analysis," IEEE Transactions Intelligent Transportation Systems **23**(8), 11465 (2022).
39. R. Khalili and K. Salamatian, "A new analytic approach to evaluation of packet error rate in wireless networks," in *3rd Annual Communication Networks and Services Research Conference (CNSR'05)*, (2005), pp. 333–338.
40. S. Wilson, *Digital Modulation and Coding* (Prentice Hall, 1996).
41. H. Kaushal, V. Jain, and S. Kar, *Free Space Optical Communication* (Springer, 2017).
42. "Propagation data required for the design of terrestrial free-space optical links," Recommendation ITU-R (2012).
43. "Prediction methods required for the design of terrestrial free-space optical links," Recommendation ITU-R (2012).
44. J. C. Ricklin, S. M. Hammel, F. D. Eaton, and S. L. Lachinova, "Atmospheric channel effects on free-space laser communication," J. Opt. Fiber Commun. Rep. **3**(2), 111–158 (2006).
45. H. Henniger and O. Wilfert, "An introduction to free-space optical communications," Radioengineering **19**, 1 (2010).
46. B.-B. Zhao, X.-G. Wang, J. Zhang, and C. Wang, "Relative intensity noise of a mid-infrared quantum cascade laser: insensitivity to optical feedback," Opt. Express **27**(19), 26639–26647 (2019).
47. S. Borri, S. Bartalini, P. C. Pastor, I. Galli, G. Giusfredi, D. Mazzotti, M. Yamanishi, and P. De Natale, "Frequency-noise dynamics of mid-infrared quantum cascade lasers," IEEE J. Quantum Electron. **47**(7), 984–988 (2011).
48. S. Bartalini, S. Borri, I. Galli, G. Giusfredi, D. Mazzotti, T. Edamura, N. Akikusa, M. Yamanishi, and P. De Natale, "Measuring frequency noise and intrinsic linewidth of a room-temperature dfb quantum cascade laser," Opt. Express **19**(19), 17996–18003 (2011).
49. H. Stern, S. Mahmoud, and L. Stern, *Communication Systems: Analysis and Design* (Pearson Prentice Hall, 2004).
50. Harvard–Smithsonian Center for Astrophysics (CfA), *The HITRAN database* (2013).
51. Harvard–Smithsonian Center for Astrophysics (CfA), V. E. Zuev Insitute of Atmosperic Optics (IAO), *HITRAN on the Web* (2019).
52. L. Rothman, I. Gordon, and Y. Babikov, *et al.*, "The HITRAN2012 molecular spectroscopic database," J. Quant. Spectrosc. Radiat. Transfer **130**, 4–50 (2013).
53. F. X. Kneizys, *Atmospheric Transmittance/Radiance, Computer Code LOWTRAN 5*, 697 (Optical Physics Division, Air Force Geophysics Laboratory, 1980).
54. S. Malik and P. K. Sahu, "Free space optics/millimeter-wave based vertical and horizontal terrestrial backhaul network for 5g," Opt. Commun. **459**, 125010 (2020).
55. M. Handura, K. Ndjavera, C. Nyirenda, and T. Olwal, "Determining the feasibility of free space optical communication in namibia," Opt. Commun. **366**, 425–430 (2016).
56. G. C. Valley, "Isoplanatic degradation of tilt correction and short-term imaging systems," Appl. Opt. **19**(4), 574–577 (1980).